Research Article
Vol. 26, No. 22 | 29 Oct 2018 | OPTICS EXPRESS 28178
Optics EXPRESS

Suppression of parasitic interference in a fiber-tip Fabry-Perot interferometer for high-pressure measurements

JINSHAN XU, JUN HE,* WEI HUANG, XIZHEN XU, KUIKUI GUO, ZHE ZHANG, AND YIPING WANG

Key Laboratory of Optoelectronic Devices and Systems of Ministry of Education and Guangdong Province, College of Optoelectronic Engineering, Shenzhen University, Shenzhen 518060, China
*hejun07@szu.edu.cn

Abstract: We demonstrate a novel design and fabrication process for fiber-tip Fabry-Perot interferometric (FTFPI) pressure sensors which eliminates fringe envelopes in the reflection spectrum. The outer facet reflectivity and thickness of the FTFPI silica diaphragm were reduced through orthogonal rough-polishing of the fiber end facet. A silica FTFPI sample with a diaphragm thickness of ~10.7 μm was produced and tested under hydraulic pressures ranging from 0 to 30 MPa. The proposed sensor achieved a pressure sensitivity of −284 pm/MPa at 1555 nm and could be a valuable new tool for high pressure measurements.

1. Introduction

Optical fiber Fabry-Perot interferometric (FPI) sensors exhibit several characteristics which have attracted attention in recent years. They have been widely investigated for applications in a variety of fields, such as environmental monitoring, biomedical instruments, and mechanical engineering [1–7]. Among these, all-silica FPIs fabricated at the tip of an optical fiber are preferable for pressure measurements due to their small size, robust mechanical structure, and high sensitivity [8–11]. Pressure sensitivity is one of the most important properties of a fiber-tip Fabry-Perot interferometric (FTFPI) sensor. As such, recent studies have mostly investigated optimal structure types for the reflecting mirrors at the fiber ends. FTFPI pressure sensitivity can be increased by reducing the mirror thickness [12–14].

Reflection occurs at three interfaces in the flat silica diaphragm, with a thickness of several to tens of microns, located at the end of a short hollow core fiber (HCF). This three-wave interference could potentially modulate the fringe envelope, affecting the measurement of peak or dip wavelengths [9] and the observation of spectral shifts [10]. To remove these unwanted reflections at the fiber end surface, Liu *et al* polished a single-mode fiber (SMF) facet to 8° [15]. Smith *et al* reported an ultra-small Fabry-Perot cavity written into optical micro-fibers, they removed the parasitic interference by cleaving the end of the micro-fiber using a focused-ion beam at an angle of 45° [16]. While oblique surfaces can reduce facet reflectivity, they can also affect the linear response of an FTFPI pressure sensor. In addition, tilting the fiber end facet is also a complex process. Hence, researchers proposed other ways to reduce the outer facet reflectivity, such as by increasing the roughness of the outer facet. For example, Xu *et al* proposed a novel diaphragm-based FPI pressure sensor which utilized hydrofluoric acid (HF) etching. Reflections from the exterior diaphragm surface can be neglected because the two surfaces are not parallel after cleaving. HF etching also produces a rough outside surface [17] and requires the use of hazardous chemicals. Sorin *et al* measured the absolute optical path differences (OPDs) between reflectors spaced along a single sensing fiber using a coherence-domain demodulation method [18]. However, this method exhibits a limited spatial resolution of ~10 μm, which is not sufficient for discriminating the parasitic interference in the FTFPIs with thin diaphragms [18,19]. Moreover, Shen *et al* proposed a

#332744 https://doi.org/10.1364/OE.26.028178
Journal © 2018 Received 31 May 2018; revised 1 Aug 2018; accepted 19 Sep 2018; published 15 Oct 2018

frequency estimation-based signal processing algorithm for multiplexed FPIs, to estimate the absolute OPDs [20]. Hence, the parasitic interference from different interfaces could easily be discriminated using this method. However, this approach always requires large computations, such as fast Fourier transformation (FFT) and/or digital filtering [21,22].

In this study, we propose a replicable technique for fabricating all-silica FTFPI high-pressure sensors, avoiding fringe envelopes in the reflection spectrum. This device is produced by polishing the FTFPI end facet. This process not only decreases diaphragm thickness, which increases sensitivity, but also reduces diaphragm reflectivity which decreases noise. A polishing experiment demonstrated the facet reflectivity of a flat-end SMF, polished using a 9-µm-grit polishing paper, could be reduced below 5% compared with normal Fresnel reflection. The proposed sensor can also eliminate the influence of fringe envelopes. A silica diaphragm was produced with a thickness of 10.7 µm, achieving a pressure sensitivity of −284 pm/MPa over an applied pressure range of 0 to 30 MPa.

2. Principles

Figure 1(a) illustrates that there are three silica/air interfaces which can reflect light along the SMF. Surface 1 is the flat-end of the SMF, surface 2 and surface 3 are the inner and outer surfaces of the silica diaphragm, respectively. The reflectivity of the silica/air interface is so low (~3.5%) that we can neglect the impact of high-order FP interference. The total reflected electric field E and light intensity I can then be expressed as:

$$
\begin{aligned}
E &= E_1 - E_2 \exp\left[j\left(\frac{4\pi}{\lambda} n_a L \right) \right] + E_3 \exp\left[j\left(\frac{4\pi}{\lambda} \left(n_s d + n_a L \right) \right) \right], \\
I &= E \cdot E^* = E_1^2 + E_2^2 + E_3^2 - 2E_1E_2 \cos\left(\frac{4\pi}{\lambda} n_a L \right) \\
&\quad \underbrace{-2E_2E_3 \cos\left(\frac{4\pi}{\lambda} n_s d \right) + 2E_1E_3 \cos\left[\frac{4\pi}{\lambda} \left(n_s d + n_a L \right) \right]}_{\text{Parasitic Interference}},
\end{aligned}
\tag{1}
$$

where E_1, E_2, and E_3 are the field amplitudes of the light reflected by surface 1, surface 2, and surface 3, respectively. L is the length of the air cavity, n_a and n_s are the refractive indexes of air and silica, respectively, d is the thickness of the silica diaphragm, and λ is the wavelength of the light.

As shown in Eq. (1), the existence of E_3 will introduce the parasitic interference. E_3 can increase or decrease the intensity of the reflected light, modulating the reflection spectrum by inducing a fringe envelope. Fig. 1(b) illustrates the measured FTFPI spectrum from 1250 to 1650 nm, in which the 0 dB level corresponds to a fiber end facet Fresnel reflection of ~3.5%. The FTFPI spectrum has a periodic fringe envelope, clearly showing the modulation caused by E_3 [23,24]. Unlike in two-beam interference, this envelope can be used to determine the thickness of the silica diaphragm [25]. However, this modulated spectrum can lead to errors when estimating the actual cavity length L, by tracing the interfering minima or maxima in the spectrum [12]. Furthermore, low fringe contrast near the envelope valley may limit the use of spectrum demodulation, which is commonly applied in optical signal processing.

The effects of the fringe envelope can be lessened by reducing the thickness of the silica diaphragm. When the silica is sufficiently thin, the envelope can be considered as the result of interference between surface 2 and surface 3. The interval between two adjacent valleys (or peaks) in the envelope can be expressed as $\lambda^2/2n_sd$ [26]. Recently, we reported an FTFPI silica diaphragm with a thickness of below 180 nm [13]. The fringe envelope spacing in the reflection spectrum was larger than 2120 nm. The resulting modulated spectrum is difficult to measure using standard equipment. However, FTFPIs with ultra-thin diaphragms are not suitable for high-pressure applications.

Optics EXPRESS

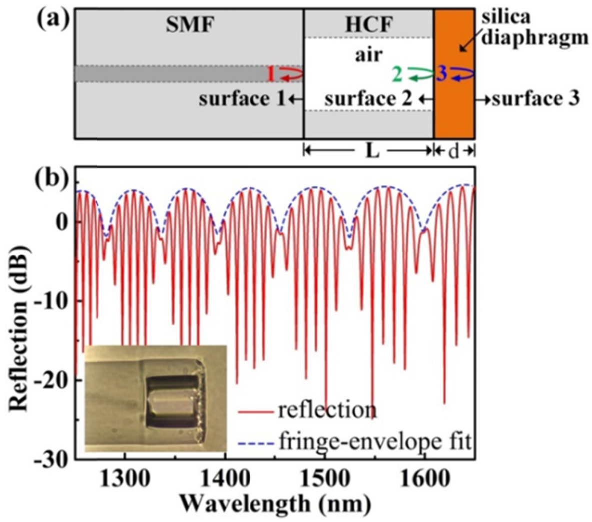

Fig. 1. A schematic diagram of the FPI with a silica diaphragm. (b) The measured multi-beam interference spectrum for the FTFPI sample fabricated without rough-polishing. Inset: a microscope image of the FTFPI sample.

In addition to decreasing diaphragm thickness, the effects of the fringe envelope can be lessened by reducing the amplitude of light reflected by surface 3 (E_3). If E_3 tends to 0, Eq. (1) becomes:

$$I = E_1^2 + E_2^2 - 2E_1E_2\cos\left(\frac{4\pi}{\lambda}n_a L\right) \qquad (\text{if} E_3 \to 0) \tag{2}$$

This represents a pure two-beam interference in which the FTFPI reflection spectrum does not include a fringe envelope, regardless of diaphragm thickness.

The amplitude of the light reflected by surface 3 (E_3) can be reduced in a variety of ways, such as applying an index matching material to the fiber end [27] or applying an angled silica diaphragm to the end facet [15, 16, 28, 29]. However, the temperature dependence of the index matching material has a significant influence on the amplitude of the reflected light, and the titled facet of the silica diaphragm will affect the linear pressure response of the FTFPI. In this paper, we increased the roughness of the fiber end face through orthogonal polishing, and hence the facet reflectivity was significantly reduced.

3. Device fabrication

Figures 2(a1–5) illustrate the five steps involved in FTFPI fabrication. In step 1 (a1), the cleaved ends of an SMF and an HCF (INNOSEP-TSP075150) were fastened to the left and right motors of a commercial fusion splicer (Fujikura FSM-80S). Each had an outer diameter of 125 μm and an inner diameter of 75 μm. They were then spliced together using an electrical arc discharge with a standard −30 bit fusion power and a fusion time of 800 ms. In step 2 (a2), the HCF was trimmed using a fiber micro-cutting system to shorten the length of the remaining HCF, which integrates with the SMF to ~100 μm. The fiber micro-cutting system, shown in Fig. 2(b), is described in detail below. In step 3 (a3), the trimmed ends of the SMF and SMF-HCF samples obtained from the first two steps were spliced together using an electrical arc discharge with a standard −25 bit fusion power and a fusion time of 600 ms. The result is a normal in-fiber FPI. Fig. 2(c) displays a microscope image of the in-fiber FPI produced in step 3. In step 4 (a4), the in-fiber FPI was trimmed using a fiber micro-cutting system to decrease the SMF length on the side of the HCF for FTFPI fabrication. The fiber micro-cutting system exhibited promising accuracy in reducing the length of the remaining

SMF to ~20 μm, to form a silica diaphragm. However, in considering the mechanical strength of SMF-HCF fusion splices, we elected to control the length of the remaining SMF to ~40 μm. Fig. 2(d) illustrates a microscope image of the FTFPI. Finally, in step 5 (a5), the fiber-tip FPI was placed in the fiber lensing machine (ULTRAPOL) for the polishing of FTFPI surface 3, to reduce reflectivity and decrease silica diaphragm thickness. Fig. 2(e) partially illustrates the fiber end face polishing machine, which is described in detail below, and the experimental configuration for monitoring the reflection interference spectrum of the polished FTFPI. This setup contained a 3 dB coupler, a broadband light source (BBS, Fiber-Lake FL-ASE-EB) and an optical spectrum analyzer (OSA, Yokogawa AQ6370C). The BBS was based on amplified spontaneous emission (ASE) of four-channel semiconductor optical amplifiers (SOAs), and had a wavelength range from 1250 to 1650 nm (i.e. a bandwidth of 400 nm), an output power of 10.79 dBm, a power stability of ± 0.02 dB, and a degree of polarization (DOP) of less than 5%. The OSA was scanned from 1250 to 1650 nm with a wavelength resolution set to be 0.1 nm and a 'HIGH1' sensitivity mode.

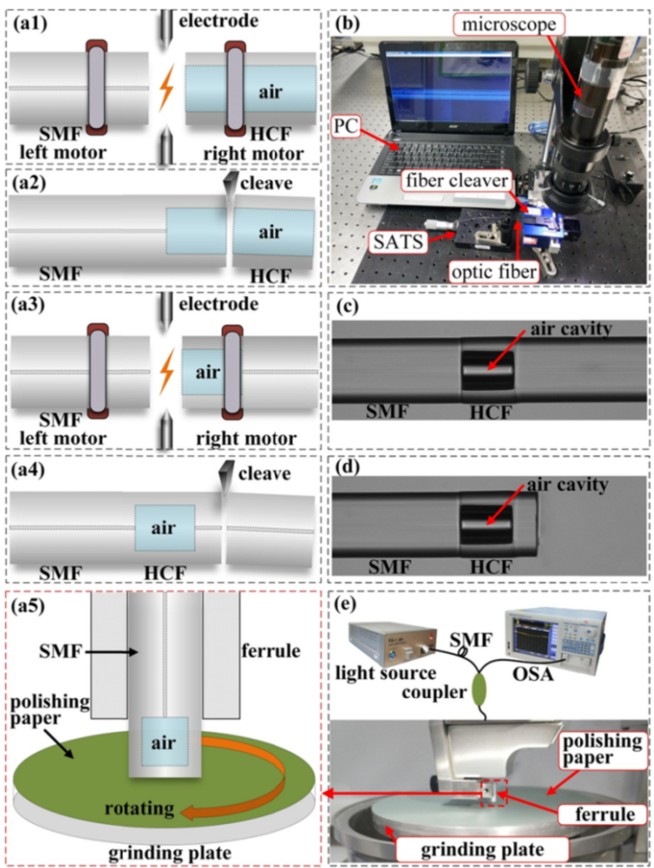

Fig. 2. (a1–a5) Schematic diagrams of the fabrication process for fiber-tip FPIs without multi-beam interference. (b) A photograph of the fiber micro-cutting system. (c) A microscope image of the in-fiber FPI. (d) A microscope image of the fabricated FTFPI. (e) The experimental setup used for FTFPI polishing.

As mentioned previously, the fiber micro-cutting system included a CCD camera used to capture images of the fiber sample positioned on the fiber cleaver, a computer to display enlarged sample images transmitted from the CCD, a lifting platform to dynamically adjust focus by raising and lowering the camera, a fiber cleaver, and a single-axis translational stage (SATS, PT1, THORLABS) with a 25 mm travel range and engraved graduations every 10 μm. One end was clamped to the fiber cleaver and the other was fixed to the fiber holder, which was integrated with a one-dimensional displacement platform. We could then shift the sample to adjust the space between the sample and fiber cleaver blade, to identify the optimal cutting location. This spatial adjustment process was displayed on the computer.

The fiber end face polishing machine contained an aluminum carrier plate used to hold abrasive polishing paper during the polishing of bare fibers. This plate could then be driven by an electromotor and rotated clockwise or counterclockwise. Abrasive polishing paper of varying grit sizes could be used as needed. The setup also included a ceramic ferrule to keep the fiber still during the polishing process, a 1-micron micro-positioner to precisely adjust the fiber height, and a digital angle dial for setting and reading desired angles for polishing of the bare fiber ends. In this experiment, the angle was set at 0° to ensure the fiber end facet was parallel to the polishing paper. The fiber could then be fixed tightly using a clamp in the fiber end face polishing machine. The aluminum carrier plate, abrasive polishing paper, and ceramic ferrule are shown in Fig. 2(e).

4. Parasitic interference suppression via rough-polishing

4.1 Fiber end rough-polishing for facet reflectivity reduction

We experimentally polished the cut end of an SMF with three types of polishing paper. Figs. 3(a1), 3(b1), and 3(c1) show the smooth SMF end facet after being polished by 1-μm, 3-μm, and 9-μm grit polishing paper, respectively. Figs. 3(a2), 3(b2), and 3(c2) show enlarged sections of this end facet and demonstrate the varying roughness of the polished surface. This roughness varies significantly, particularly for the facet polished by 9-μm-grit polishing paper. Additionally, the reflective properties of these three polished facets were tested experimentally. Figs. 3(a3), 3(b3), and 3(c3) display the reflection spectra for the three samples for wavelengths ranging from 1250 nm to 1650 nm. It should be noted that the 0 dB level in Fig. 3 was measured with respect to a fiber end facet Fresnel reflection of ~3.5%.

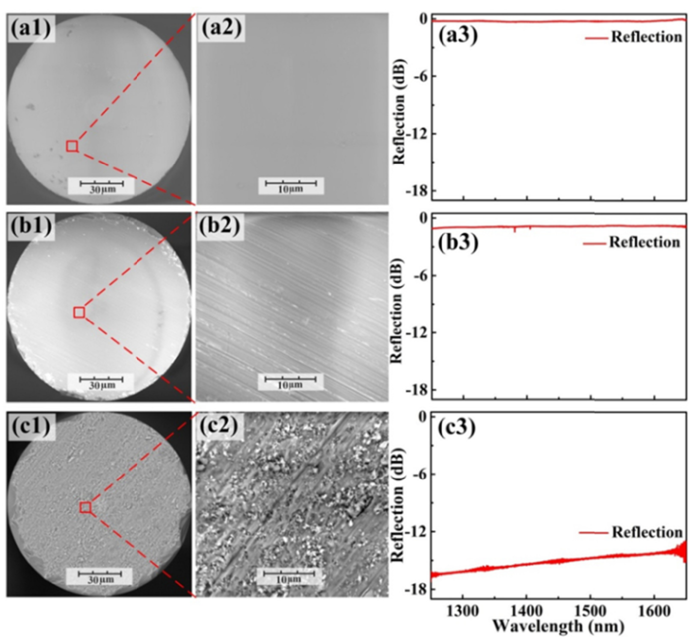

Fig. 3. SEM images of the SMF end facet polished by 1-μm (a1), 3-μm (b1), and 9-μm (c1) grit polishing paper, including their respective enlarged partial views (a2–c2). Also shown are the reflection spectra for the SMF polished by 1-μm (a3), 3-μm (b3), and 9-μm (c3) grit polishing paper.

Fig. 3(a3) demonstrates that the loss of reflection was less than 0.35 dB. This suggests the 1-μm-grit polishing paper had almost no effect on reducing the reflectivity of the SMF. This was also observed indirectly in the enlarged partial SEM micrograph image shown in Fig. 2(a2). Fig. 3(b3) demonstrates that the loss of reflection for the facet polished by 3-μm-grit polishing paper was no less than 1.1 dB (i.e., the facet reflectivity was reduced to 2.7%). However, by analyzing the reflection spectrum and micrograph in Fig. 3, it is clear that the 9-μm-grit polishing paper can damage the SMF end facet. The loss of light reflection exceeds 13 dB at the wavelength of 1550 nm (i.e., the facet reflectivity was reduced to 0.2%).

4.2 Parasitic interference suppression in FTFPIs via rough-polishing

We investigated the effects of FTFPI after polishing with various paper types. Three FTFPI samples (samples 1, 2, and 3) were fabricated in five steps using polishing paper with 1-μm, 3-μm, and 9-μm grit, respectively. Figs. 4(b), 4(c), and 4(d) illustrate the corresponding reflection interference spectra. Fig. 4(a) shows the spectrum of an ordinary in-fiber FPI for comparison. It should be noted that the 0 dB in Fig. 4 represents a fiber end Fresnel reflection of ~3.5%. The modulation of the fringe envelope is evident in the reflection interference spectrum for FTFPI samples 1 and 2, as the polishing paper slightly decrease the reflectivity of FTFPI surface 3. As shown in Fig. 4(d), FTFPI sample 3 nearly eliminates the fringe envelope, as expected previously. This is because the grinding process significantly reduced the reflectivity of FTFPI surface 3, as analyzed in Fig. 3(c3). There is no fringe envelope in the reflection spectrum to use for estimating diaphragm thickness during the polishing of sample 3. As such, we must polish the sample using 3-μm-grit polishing paper in order to thin the diaphragm to a thickness of ~11 μm. The 9-μm paper is then used to carefully polish the sample until the fringe envelope in its reflection spectrum is eliminated.

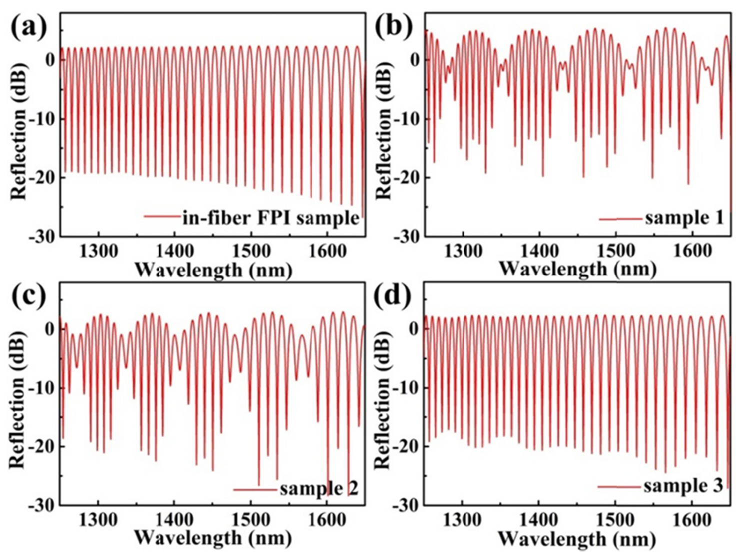

Fig. 4. (a) The interference spectrum for a general in-fiber FPI. (b), (c), and (d) The multi-beam interference spectra of fiber-tip FPIs polished by1-μm, 3-μm, and 9-μm grit polishing paper, respectively.

An FTFPI pressure sensor (sample 3) was fabricated without a fringe envelope in its reflection spectrum. Fig. 5(a) shows a microscope image of the resulting FTFPI. One end of the short HCF length was spliced with an SMF end to form an air cavity. The other HCF end was sealed with a silica diaphragm formed by fusion splicing and polishing. Fig. 5(b) shows the outer facet of the silica diaphragm, rough-polished with 9-μm-grit polishing paper. The diaphragm was fractured with femtosecond laser in order to accurately measure the thickness

Optics EXPRESS

of the silica diaphragm. Fig. 5(c) shows an SEM image of the fractured diaphragm, with a measured thickness of ~10.7 μm as shown in the inset. Although it is too thick to provide high pressure sensitivity, it can eliminate fringe envelopes in the reflection spectrum and has potential for high pressure applications.

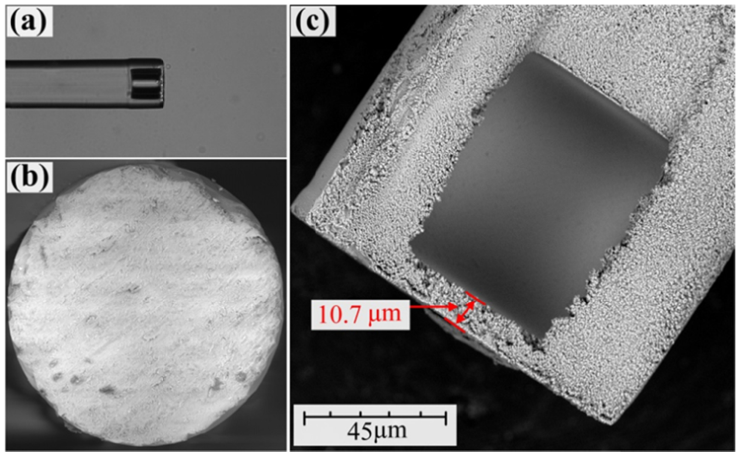

Fig. 5. (a) A microscope image of the FTFPI polished by 9-μm-grit polishing paper. (b) An SEM image of the silica diaphragm at the top end of the FTFPI. (c) An enlarged SEM image of a fractured end of the FTFPI with a silica diaphragm thickness of ~10.7 μm.

5. High-pressure response

We investigated the response of sample 3 to hydraulic pressures varying from 0 to 30 MPa in increments of 2 MPa, remaining at each step for 5 min. As explained previously, there was no fringe envelop in the reflection spectrum of the two samples. As such, we can easily monitor random interference valleys to investigate the relationship between wavelength shift and increasing pressure. The positions of the interference valleys for sample 3 at ~1555.3 nm correspond to various applied pressures, as illustrated in Fig. 6(a). The 0 dB level in Fig. 6(a) corresponds to a fiber end Fresnel reflection of ~3.5%. The corresponding wavelength shift of these interference valleys, in response to varying pressure, is plotted in Fig. 6(b). It is evident that increasing pressure causes the dip wavelength in the interference spectrum to shift linearly towards a shorter wavelength (i.e. 'blue' shift). Additionally, sample 3 achieved a pressure sensitivity of −284 pm/MPa.

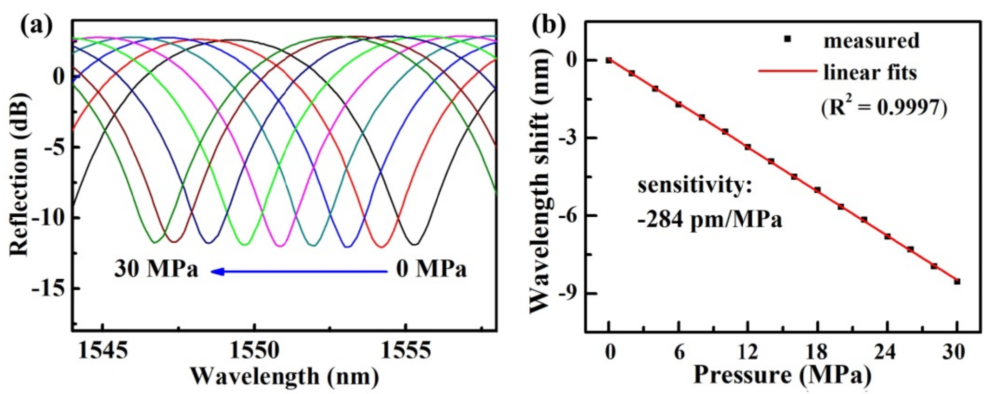

Fig. 6. (a) Reflection spectral evolution for the FTFPI as hydraulic pressure increased from 0 to 30 MPa. (b) The wavelength shift of the interference dip wavelength as a function of the applied hydraulic pressure.

Optics EXPRESS

6. Conclusion

The fabrication process for an FTFPI pressure sensor without a fringe envelope in its reflection spectrum was proposed and experimentally demonstrated. The reflectivity of the end surface was reduced by polishing the outer facet of an FTFPI silica diaphragm, using 9-μm-grit polishing paper, to a thickness of 10.7 μm. A high pressure response was observed from 0 to 30 MPa with a sensitivity of ~–284 pm/MPa. The benefits of this all-silica FTFPI include low fabrication cost, avoidance of a fringe envelope, high mechanical strength, and significant pressure endurance. As such, the proposed FTFPI device is an excellent candidate for performing pressure measurements in harsh environments.

7. Funding

National Natural Science Foundation of China (NSFC) (61505120, 61425007, 61635007); Natural Science Foundation of Guangdong Province (2017A010102015, 2015B010105007, 2014A030308007); Shenzhen Science and Technology Innovation Commission (JCYJ20170412105604705, JCYJ20170302143105991, JCYJ20160427104925452); Research Funding from Shenzhen University (2017019); Development and Reform Commission of Shenzhen Municipality Foundation.

References

1. M. Quan, J. Tian, and Y. Yao, "Ultra-high sensitivity Fabry-Perot interferometer gas refractive index fiber sensor based on photonic crystal fiber and Vernier effect," Opt. Lett. **40**(21), 4891–4894 (2015).
2. B. H. Lee, Y. H. Kim, K. S. Park, J. B. Eom, M. J. Kim, B. S. Rho, and H. Y. Choi, "Interferometric fiber optic sensors," Sensors (Basel) **12**(3), 2467–2486 (2012).
3. K. Yang, J. He, Y. Wang, S. Liu, C. Liao, Z. Y. Li, G. L. Yin, B. Sun, and Y. P. Wang, "Ultrasensitive temperature sensor based on a fiber Fabry-Perot interferometer created in a mercury-filled silica tube," IEEE Photonics J. **7**(6), 6803509 (2015).
4. J. R. Zhao, X. G. Huang, W. X. He, and J. H. Chen, "High-resolution and temperature-insensitive fiber optic refractive index sensor based on fresnel reflection modulated by Fabry-Perot interference," J. Lightwave Technol. **28**(19), 2799–2803 (2010).
5. M. S. Ferreira, L. Coelho, K. Schuster, J. Kobelke, J. L. Santos, and O. Frazão, "Fabry-Perot cavity based on a diaphragm-free hollow-core silica tube," Opt. Lett. **36**(20), 4029–4031 (2011).
6. Z. Zhang, C. Liao, J. Tang, Z. Bai, K. Guo, M. Hou, J. He, Y. Wang, S. Liu, F. Zhang, and Y. P. Wang, "High-sensitivity gas-pressure sensor based on fiber-tip PVC diaphragm Fabry-Perot interferometer," J. Lightwave Technol. **35**(18), 4067–4071 (2017).
7. S. Liu, K. Yang, Y. Wang, J. Qu, C. Liao, J. He, Z. Li, G. Yin, B. Sun, J. Zhou, G. Wang, J. Tang, and J. Zhao, "High-sensitivity strain sensor based on in-fiber rectangular air bubble," Sci. Rep. **5**(1), 7624 (2015).
8. D. Donlagic and E. Cibula, "All-fiber high-sensitivity pressure sensor with SiO2 diaphragm," Opt. Lett. **30**(16), 2071–2073 (2005).
9. Y. Z. Zhu and A. B. Wang, "Miniature fiber-optic pressure sensor," IEEE Photonics Technol. Lett. **17**(2), 447–449 (2005).
10. W. Wang, N. Wu, Y. Tian, C. Niezrecki, and X. Wang, "Miniature all-silica optical fiber pressure sensor with an ultrathin uniform diaphragm," Opt. Express **18**(9), 9006–9014 (2010).
11. J. C. Xu, G. Pickrell, X. W. Wang, W. Peng, K. Cooper, and A. B. Wang, "A novel temperature-insensitive optical fiber pressure sensor for harsh environments," IEEE Photonics Technol. Lett. **17**(4), 870–872 (2005).
12. Y. Z. Zhu, K. L. Cooper, G. R. Pickrell, and A. Wang, "High-temperature fiber-tip pressure sensor," J. Lightwave Technol. **24**(2), 861–869 (2006).
13. S. Liu, Y. Wang, C. Liao, Y. Wang, J. He, C. Fu, K. Yang, Z. Bai, and F. Zhang, "Nano silica diaphragm in-fiber cavity for gas pressure measurement," Sci. Rep. **7**(1), 787 (2017).
14. X. Wang, J. Xu, Y. Zhu, K. L. Cooper, and A. Wang, "All-fused-silica miniature optical fiber tip pressure sensor," Opt. Lett. **31**(7), 885–887 (2006).
15. B. Liu, J. Lin, H. Liu, Y. Ma, L. Yan, and P. Jin, "Diaphragm based long cavity Fabry-Perot fiber acoustic sensor using phase generated carrier," Opt. Commun. **382**, 514–518 (2017).
16. S. C. Warren-Smith, R. M. Andre, J. Dellith, T. Eschrich, M. Becker, and H. Bartelt, "Sensing with ultra-short Fabry-Perot cavities written into optical micro-fibers," Sens. Actuators B Chem. **244**, 1016–1021 (2017).
17. J. Xu, X. Wang, K. L. Cooper, and A. Wang, "Miniature all-silica fiber optic pressure and acoustic sensors," Opt. Lett. **30**(24), 3269–3271 (2005).
18. W. V. Sorin and D. M. Baney, "Multiplexed sensing using optical low-coherence reflectometry," IEEE Photonics Technol. Lett. **7**(8), 917–919 (1995).

Optics EXPRESS

19. Y. P. Wang, J. P. Chen, X. W. Li, X. H. Zhang, J. X. Hong, and A. L. Ye, "Simultaneous measurement of various optical parameters in a multilayer optical waveguide by a Michelson precision reflectometer," Opt. Lett. **30**(9), 979–981 (2005).
20. F. Shen and A. Wang, "Frequency-estimation-based signal-processing algorithm for white-light optical fiber Fabry-Perot interferometers," Appl. Opt. **44**(25), 5206–5214 (2005).
21. T. Liu and G. F. Fernando, "A frequency division multiplexed low-finesse fiber optic Fabry–Perot sensor system for strain and displacement measurements," Rev. Sci. Instrum. **71**(3), 1275–1278 (2000).
22. Y. Jiang, "Fourier transform white-light interferometry for the measurement of Fiber-Optic Extrinsic Fabry–Pérot interferometric sensors," IEEE Photonics Technol. Lett. **20**(2), 75–77 (2008).
23. X. Z. Xu, Y. Wang, S. Liu, C. R. Liao, J. He, J. R. Lian, and Y. P. Wang, "Growth dynamics of ZnO nanowire on a fiber-tip air bubble," Opt. Mater. Express **7**(9), 3433–3440 (2017).
24. J. Ma, J. Ju, L. Jin, and W. Jin, "A compact fiber-tip micro-cavity sensor for high-pressure measurement," IEEE Photonics Technol. Lett. **23**(21), 1561–1563 (2011).
25. C. Liao, S. Liu, L. Xu, C. Wang, Y. Wang, Z. Li, Q. Wang, and D. N. Wang, "Sub-micron silica diaphragm-based fiber-tip Fabry-Perot interferometer for pressure measurement," Opt. Lett. **39**(10), 2827–2830 (2014).
26. S. Liu, Y. Wang, C. Liao, G. Wang, Z. Li, Q. Wang, J. Zhou, K. Yang, X. Zhong, J. Zhao, and J. Tang, "High-sensitivity strain sensor based on in-fiber improved Fabry-Perot interferometer," Opt. Lett. **39**(7), 2121–2124 (2014).
27. M. Kihara, S. Nagasawa, and T. Tanifuji, "Return loss characteristics of optical fiber connectors," J. Lightwave Technol. **14**(9), 1986–1991 (1996).
28. S. Nagasawa, Y. Yokoyama, F. Ashiya, and T. Satake, "A high-performance single-mode multifiber connector using oblique and direct endface contact between multiple fibers arranged in a plastic ferrule," IEEE Photonics Technol. Lett. **3**(10), 937–939 (1991).
29. M. Kihara, S. Nagasawa, and T. Tanifuji, "Design and performance of an angled physical contact type multifiber connector," J. Lightwave Technol. **14**(4), 542–548 (1996).